

Dispersion Analysis in Hypersonic Flight During Planetary Entry Using Stochastic Liouville Equation

Abhishek Halder* and Raktim Bhattacharya†

Texas A&M University, College Station, Texas 77843-3141

DOI: 10.2514/1.51196

A framework is provided for the propagation of uncertainty in planetary entry, descent, and landing. The traditional Monte-Carlo based dispersion analysis is overly resource-expensive for such high-dimensional nonlinear systems and does not provide any methodical way to analyze the effect of uncertainty for mission design. It is shown that propagating the density function through Liouville equation is computationally attractive and suitable for further statistical analysis. Comparative simulation results are provided to bring forth the efficacies of the proposed method. Examples are given from the entry, descent, and landing domain to illustrate how one can retrieve statistical information of interest from an analyst's perspective.

Nomenclature

B_c	= ballistic coefficient
$\frac{C_L}{C_D}$	= lift-to-drag ratio
\mathbf{F}	= augmented dynamics vector
\mathbf{f}	= dynamics vector
g	= acceleration due to gravity $\frac{GM}{(R_0+h)^2}$, where GM is the Gravitational constant for Mars
h	= altitude
n_s	= number of states
n_p	= number of parameters
\mathbf{p}	= parameter vector
R_0	= mean equatorial radius of Mars
t	= time
V	= Mars-relative velocity
v_c	= normalizing velocity constant $= \sqrt{\frac{\mu}{R_0}}$, where $\mu = gR_0^2$
\mathbf{X}	= augmented state vector
\mathbf{x}	= state vector
γ	= flight-path angle
ξ	= latitude
λ	= longitude
ρ	= Martian atmospheric density
ρ_0	= reference-level density
σ	= bank angle
φ	= probability density function
χ	= velocity azimuth angle measured from North
Ψ	= trace of the Jacobian of the dynamics
Ω	= rotational angular velocity for Mars

Subscript

i	= variable number
-----	-------------------

I. Introduction

WITH the need to develop next generation entry, descent, and landing (EDL) technologies for planetary exploration, quantification of uncertainties have become a major technical challenge for space system simulations. In particular, Mars EDL technologies

Received 17 June 2010; revision received 24 September 2010; accepted for publication 27 September 2010. Copyright © 2010 by Abhishek Halder. Published by the American Institute of Aeronautics and Astronautics, Inc., with permission. Copies of this paper may be made for personal or internal use, on condition that the copier pay the \$10.00 per-copy fee to the Copyright Clearance Center, Inc., 222 Rosewood Drive, Danvers, MA 01923; include the code 0731-5090/11 and \$10.00 in correspondence with the CCC.

*Graduate Student, Department of Aerospace Engineering; ahalder@tamu.edu. Member AIAA.

†Assistant Professor, Department of Aerospace Engineering; raktim@tamu.edu. Member AIAA.

are witnessing a paradigm shift as we strive for increasing the landing mass capability at a higher surface elevation (lower atmospheric density) while improving the landing accuracy. Future missions including Mars Science Laboratory (MSL), Mars Sample Return (MSR), and Astrobiology Field Laboratory (AFL) are pushing the EDL technology limits toward the aforesaid directions to pave the way for human exploration missions. As pointed out in [1,2], from 1976 to 2008, all six NASA missions which landed successfully on Mars, were based on Viking-era EDL technologies characterized by landing mass of less than 600 kg, landing elevation of less than -1.4 km Mars Orbiter Laser Altimeter (MOLA) reference with landing footprint uncertainty in hundreds of km. In fact, they all had similar design attributes, e.g., 70° sphere-cone aeroshell, supersonic Disk-Gap-Band (DGB) parachutes with diameter less than the Viking 16 m design and SLA-561V thermal protection system (TPS). In contrast, the MSL mission, scheduled to launch in 2011, has a higher landing mass, higher surface elevation for landing, an order of magnitude improvement in landing footprint uncertainty, a larger DGB parachute and a new TPS. Braun and Manning [1] have listed the probable future directions of EDL technological pursuits and challenges thereof. To achieve such technical readiness level, development of these new generation of landers will require very high-fidelity simulations enabling the assessment of risk and incorporating that knowledge for the purpose of robust mission design supported by statistical verification and validation. More precisely, a probabilistic quantification of being inside or outside some predefined operational safety margin is sought that can account the associated uncertainties in initial conditions and system parameters resulting off-nominal trajectories.

Traditionally, a Monte-Carlo (MC) based dispersion analysis is carried out for this purpose where one simulates a large number of trajectories for randomly sampled initial conditions and parameter values. If most or all of such trajectories remain inside the safety margin, one can at best hope for the system safety and reliability without any quantitative guarantee whatsoever. Usually the engineers responsible for subsystem models identify the uncertainty bounds and decide about the sampling strategy based on their experience. Clearly, brute force MC simulations are not the best approach for such mission critical uncertainty analysis. Moreover, for high-dimensional and nonlinear dynamics like spacecraft EDL, MC simulations are tremendously expensive as one strives to simulate individual trajectories one by one for uncertainties in hundreds of states and parameters and their combinations. In spite of all these drawbacks, almost all space mission uncertainty analysis are done with MC simulations including Mars Pathfinder [3], METEOR [4] recovery module, Stardust [5] comet sample return capsule, Mars Microprobe [6], MSP 2001 Orbiter and Lander [7] and to-be-launched MSL [8] mission. In fact, many important decisions in mission design have been historically driven by MC based dispersion analysis. Mars landing site selection [9], design of the Pathfinder

aeroshell thermal protection system [10] and parachute deployment algorithm [3] are examples for the same. This heavy bias toward MC simulations among EDL analysis practitioners is partly due to its ease of implementation and partly due to the scarcity of alternative analysis methods. Two primary EDL simulation frameworks which are seeing extensive use at present, are NASA Langley Research Center's Program to Optimize Simulated Trajectories II (POST2) [11] and NASA Jet Propulsion Laboratory's Dynamics Simulator for Entry, Descent and Surface Landing (DESENDS) [12]. Both of these two presently rely on MC based dispersion analysis for EDL simulations.

The limitations of MC based dispersion analysis are well-known [13] (see Ch. 1), i.e., poor computational scalability and lack of any coherent methodology to quantify the evolution of uncertainty in a statistically consistent manner. Consequently, researchers have pursued different methods for uncertainty propagation in dynamical systems in general while few of them have been attempted in EDL domain. In this paper, we will classify these methods in two broad categories: *parametric* (where one evolves the statistical moments) and *nonparametric propagation of uncertainty* (where one evolves the full probability density function, or PDF). There have been three major directions in parametric propagation of uncertainty as listed below.

1) The simplest method in this category assumes a *linear state space* description of the form $\dot{\mathbf{x}} = \mathbf{Ax}$, $\mathbf{x} \in \mathbb{R}^n$. With the initial condition uncertainty assumed to be *Gaussian*, one then sets for propagating the mean ($\bar{\mathbf{x}}$) and covariance (P) matrix by the well-known equations $\dot{\bar{\mathbf{x}}} = A\bar{\mathbf{x}}$ and $\dot{P} = A^T P + P A$. The computational efficiency of this method mainly depends on the efficiency of the numerical algorithm to integrate the covariance propagation equation and in some cases, may even perform worse than MC [14]. Of course, the major drawback is that a typical EDL system with large number of states involving highly nonlinear dynamics with non-Gaussian initial joint PDF is too far to fit in this framework. Nevertheless, this has been attempted in EDL problem (see [14]).

2) In *polynomial chaos* (PC) method, one derives a set of deterministic ordinary differential equations (ODEs) using either Galerkin projection [15] or the stochastic collocation [16] and then solves that set of ODEs. Although this method can handle nonlinear dynamics with non-Gaussian uncertainties, one ends up solving a higher dimensional state space problem, which becomes intractable for a realistic EDL simulation. Further, the method is difficult to apply for large nonlinearities [17] and computational performance degrades (due to finite-dimensional approximation of the probability space) if long-term statistics is desired. Recently, this method has been applied to the EDL domain [18].

3) Another method in this category is called the *direct quadrature method of moments* (DQMOM) [19] where the PDF is approximated as a sum of Dirac delta functions with evolving parameters. This method suffers from the Hausdorff moment problem [20]. There are some variations of this method where the PDF is expressed as a weighted sum of few constituent PDFs, referred to as partial PDFs, and propagates them instead of the Dirac delta functions [21].

Nonparametric propagation of uncertainties can be done in two ways: approximate method and direct method.

1) *Approximate method* is where one tries to estimate (in non-parametric sense) the underlying PDF. The method aims to approximate the solution of the PDF transport equation. This method is widely exercised in statistics community [22] under the name of *kernel density estimation*, although most applications there concern with static data. In a dynamical system, optimal values of the parameters must be determined at every instant of time. Many special cases of this, may be constructed depending on the type of kernel function and the criteria for optimization. A least-square error minimization set up is described in [23] and is shown to have good computational performance. Further generalizations are possible by considering general basis functions which are not density functions themselves. However, this too can suffer from high computational cost arising due to the explicit enforcement of normality constraint and moment closure constraint at each step of the optimization

procedure. Moreover, for high-dimensional state spaces like planetary EDL, recursively performing constrained optimization becomes extremely challenging.

2) *Direct method* is where one works with the PDF transport equation and instead of approximating its solution, strives to solve that equation directly. In the absence of process noise (which is the case we will restrict ourselves in this paper), this transport equation reduces to the *stochastic Liouville equation* (SLE) [24], which is a quasi-linear partial differential equation (PDE), first order in both space and time. This equation describes the time evolution of the joint PDF over the state space, which itself is changing due to the known dynamics. In this paper, we argue that the stochastic Liouville equation can be easily solved in such direct way using the method of characteristics (MOC). Because all the statistics can be derived from the PDF, from an information point of view, it is definitely superior than parametric propagation methods. Further, since we will be looking to solve the SLE directly, the solutions will satisfy the criteria to be PDF. Hence the problems like moment closure or normality constraints are not required to be enforced explicitly.

Our objective in this paper is to demonstrate that an MOC implementation in direct method can be computationally attractive and it does provide the necessary rigor for a statistically consistent uncertainty quantification for the EDL problem. To see why it is the case, one must realize that in solving the SLE, one propagates the joint PDF prescribed at the initial time subject to the deterministic dynamics. In MC method, one randomly picks a single initial condition and computes the trajectory and then repeats the process. In the SLE method, instead of *individual realizations* (initial conditions and/or parameters), one propagates the *ensemble of realizations*. This, in essence, means that the number density of trajectories meet the continuum hypothesis [24]. Just like the continuity equation in fluid mechanics transports the fluid mass in configuration space, the SLE transports the probability mass in phase space.

This paper is organized as follows. The SLE framework will be described in the next section along with some illustrative examples. The nonlinear Hypersonic flight dynamics model for planetary entry will be mentioned in Sec. III. Before attempting to solve the SLE for the full problem, we will describe some special cases in Sec. IV, which will provide some insight to the analysis. In Sec. V, the numerical simulations will be described. Section VI will describe how to perform further EDL specific statistical analysis and it will be shown that many typical analysis problems of EDL interest, fits nicely in the SLE framework. Section VII will conclude the paper.

II. Stochastic Liouville Equation

Consider the nonlinear autonomous state space model

$$\dot{\mathbf{x}} = \mathbf{f}(\mathbf{x}, \mathbf{p}), \quad \mathbf{x} \in \mathbb{R}^{n_s}, \quad \mathbf{p} \in \mathbb{R}^{n_p} \quad (1)$$

which can be put in an augmented form

$$\dot{\mathbf{X}} = \mathbf{F}(\mathbf{X}), \quad \mathbf{X} \in \mathbb{R}^{n_s+n_p} \quad (2)$$

where $\mathbf{X} = [\mathbf{x} \ \mathbf{p}]^T$ is the extended state space.

It is well known that under certain regularity conditions on the function \mathbf{f} , the existence and uniqueness of the solution of Eq. (1) subject to the initial condition $\mathbf{x}(0) = \mathbf{x}_0$, can be guaranteed (see theorems 3.2 and 3.3 in [25]). With mild conditions, one can also ensure that (theorems 3.4 and 3.5 in [25]) the unique solution of (1) depends continuously on \mathbf{x}_0 , \mathbf{p} and t . These properties are assumed to hold in all subsequent analysis.

Given such a deterministic function \mathbf{f} (or equivalently \mathbf{F}), the transport equation that convects the probabilistic uncertainty in the initial condition and parameters, is given by

$$\frac{\partial \varphi(\mathbf{X}, t)}{\partial t} + \sum_{i=1}^{n_s} \frac{\partial}{\partial X_i} [\varphi(\mathbf{X}, t) F_i(\mathbf{X})] = 0 \quad (3)$$

which is a quasi-linear first-order PDE with the joint PDF $\varphi(\mathbf{X}, t)$ being the dependent variable. This is the SLE which states that the spatio-temporal evolution of the joint PDF occurs in a way that

preserves the total probability mass. Put differently, if we pick up a control volume in the (extended) state space, the net flux of probability mass must be zero provided no realizations are created or destroyed (no source or sink), which holds true since all realizations start from the same initial condition [24]. SLE can be seen as the transport equation associated with the Perron-Frobenius (PF) operator [26].

A. Method of Characteristics

In this section, we briefly describe the MOC and show how that helps in reducing a linear or quasi-linear PDE to an ODE along the characteristics. Application of MOC to nonlinear PDEs can be found in [27].

Consider a PDE of the form

$$\sum_{i=1}^n a_i(z_1, z_2, \dots, z_n, \mathcal{U}) \frac{\partial \mathcal{U}}{\partial z_i} = \Gamma(z_1, z_2, \dots, z_n, \mathcal{U}) \quad (4)$$

with \mathcal{U} being the dependent variable and z_1, z_2, \dots, z_n are the n independent variables. The characteristic curves corresponding to Eq. (4) are given by the Lagrange–Charpit equations [28]

$$\begin{aligned} \frac{dz_1}{a_1(z_1, z_2, \dots, z_n, \mathcal{U})} &= \frac{dz_2}{a_2(z_1, z_2, \dots, z_n, \mathcal{U})} \\ &= \dots = \frac{dz_n}{a_n(z_1, z_2, \dots, z_n, \mathcal{U})} = \frac{d\mathcal{U}}{\Gamma(z_1, z_2, \dots, z_n, \mathcal{U})} \end{aligned} \quad (5)$$

Geometrically, this means that the $(n+1)$ dimensional vector field

$$\mathcal{F} := (a_1(z_1, z_2, \dots, z_n, \mathcal{U}), a_2(z_1, z_2, \dots, z_n, \mathcal{U}), \dots, a_n(z_1, z_2, \dots, z_n, \mathcal{U}), \Gamma(z_1, z_2, \dots, z_n, \mathcal{U}))$$

is tangent to the surface $\mathcal{U} = \mathcal{U}(z_1, z_2, \dots, z_n) \forall \{z_1, z_2, \dots, z_n\}^T \in \mathbb{R}^n$. In other words, the solution of the PDE (4) is an $(n+1)$ dimensional surface $\mathcal{U}(z_1, z_2, \dots, z_n)$ and it can be constructed as the union of the integral curves [or characteristic curves given by Eq. (5)] of the vector field \mathcal{F} .

To derive the characteristic curves for the SLE, we put Eq. (3) in a form similar to Eq. (4) (using product rule of differentiation)

$$\left(\sum_{i=1}^{n_s} F_i(\mathbf{X}) \frac{\partial \varphi(\mathbf{X}, t)}{\partial X_i} \right) + \frac{\partial \varphi(\mathbf{X}, t)}{\partial t} = -\varphi(\mathbf{X}, t) \sum_{i=1}^{n_s} \frac{\partial F_i(\mathbf{X})}{\partial \mathbf{X}_i} \quad (6)$$

From Eq. (5), it readily follows that the characteristic curves for Eq. (6) are given by

$$\frac{d\mathbf{X}_1}{F_1} = \frac{d\mathbf{X}_2}{F_2} = \dots = \frac{d\mathbf{X}_{n_s}}{F_{n_s}} = \frac{dt}{1} = \frac{d\varphi(\mathbf{X}, t)}{-\varphi(\mathbf{X}, t) \sum_{i=1}^{n_s} \frac{\partial F_i}{\partial \mathbf{X}_i}} \quad (7)$$

The equation above shows that the characteristic curves for the SLE are nothing but the trajectories of the dynamics given by Eq. (2).

B. Solution Methodology

It can be noted from Eq. (7) that using MOC, along the trajectory, one can reduce the SLE to an ODE of the form

$$\frac{d\varphi(\mathbf{X}, t)}{dt} = -\varphi(\mathbf{X}, t)\Psi(\mathbf{X}) \quad (8)$$

where $\Psi(\mathbf{X}) := \sum_{i=1}^{n_s} \frac{\partial F_i}{\partial \mathbf{X}_i}$ is the trace of the Jacobian of the underlying dynamics and hence, evolves with time. At this point, it is apparent that if the initial state and parametric uncertainties are specified in terms of a joint PDF $\varphi_0 := \varphi(\mathbf{X}(0), 0)$, then one can write the solution of Eq. (8) as

$$\varphi(\mathbf{X}, t) = \varphi_0 \exp\left(-\int_0^t \Psi(\mathbf{X}(\tau)) d\tau\right) \quad (9)$$

The exponential in Eq. (9) is formally known as the *ordered exponential* [29] and is analogous to the Dyson operator of the

quantum Liouville equation [30] in statistical quantum mechanics. Because the ordered exponential is a ratio of the instantaneous and initial PDFs, one may interpret it as a likelihood ratio [31].

It can be observed that $\Psi(\mathbf{X}(t))$ is the divergence of the vector field and hence, is a measure of the rate of change of the phase space (Lebesgue) volume. For example, if \mathbf{F} is linear time invariant, then Ψ must be a constant. Depending on the sign of this constant, the phase space volume can expand (expanding flow) or contract (contractive flow) exponentially fast or may remain constant (volume-preserving flow). The Liouville Theorem [32] tells us that the case of divergence-free vector field ensures that the system is Hamiltonian. Notice that a nonlinear vector field can be Hamiltonian too.

In general, it is hardly possible to evaluate the integral in Eq. (9) analytically and thus mandates numerical solution. Once the solution for the joint PDF $\varphi(\mathbf{X}, t)$ is obtained, one can find the marginal PDFs by integrating out the other states over their respective domains, namely

$$\varphi(X_i, t) = \int_{D_1} \dots \int_{D_{i-1}} \int_{D_{i+1}} \dots \int_{D_{n_s}} \varphi(\mathbf{X}, t) dX_1 \dots dX_{i-1} dX_{i+1} \dots dX_{n_s} \quad (10)$$

where D_i is the domain of the i th state variable at time t . Here it is important to realize that since the domain in the state space is deforming with time, one must know the instantaneous domain to carry out the integration in Eq. (10). This will be explained in more details later in the paper.

C. Illustrative Examples

We now provide some examples to clarify the ideas presented above. Specifically, we want to illustrate how MOC enables the solution of SLE (which is a PDE) by solving ODE initial value problem along the trajectories.

1. 1-D Example

Let us consider the simple 1-D dynamics [31] given by $\dot{x} = -x^2$ with initial condition $x(0) = x_0$. Then the solution of this initial value problem is given by

$$x(x_0, t) = \frac{x_0}{1 + tx_0} \quad (11)$$

Consequently, we have

$$\begin{aligned} \Psi(x(t)) &= -2x(t) = -\frac{2x_0}{1 + tx_0} \\ &\Rightarrow \exp\left(-\int_0^t \Psi(x(\tau)) d\tau\right) = \exp\left(2x_0 \int_0^t \frac{d\tau}{1 + \tau x_0}\right) \\ &= (1 + tx_0)^2 \end{aligned} \quad (12)$$

which, from Eq. (9), leads to

$$\varphi(x, t) = \varphi_0(x_0)(1 + tx_0)^2 \quad (13)$$

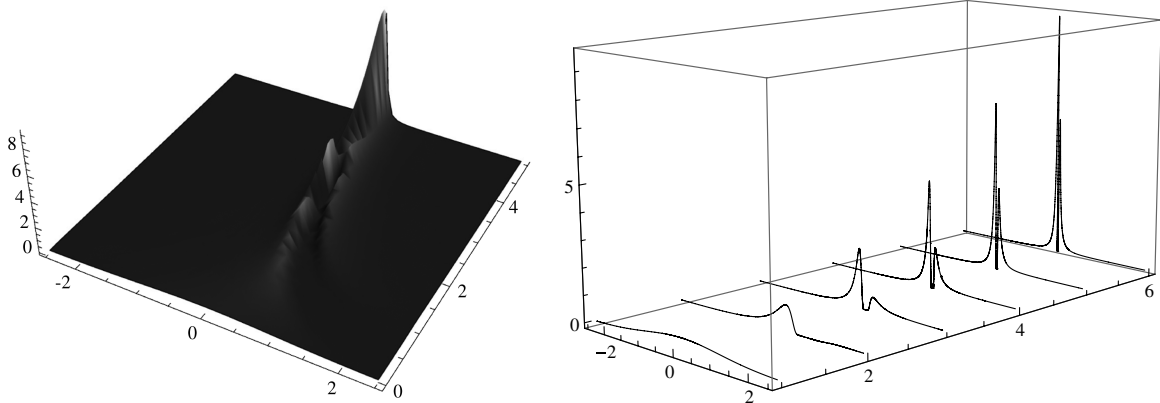
Now we can find $x_0 = x_0(x, t)$ using Eq. (11) as

$$x_0 = \frac{x}{1 - tx} \quad (14)$$

and substitute this to Eq. (13) to yield

$$\varphi(x, t) = \varphi_0\left(\frac{x}{1 - tx}\right)\left(1 + \frac{tx}{1 - tx}\right)^2 = \frac{\varphi_0(\frac{x}{1 - tx})}{(1 - tx)^2} \quad (15)$$

Figure 1 shows the spatio-temporal evolution of the PDF $\varphi(x, t)$ according to Eq. (15), when the initial PDF is chosen to be a standard normal distribution. The surface plot in Fig. 1a illustrates the rise of the PDF peak with time, accompanied with a shrinkage of its support. As Fig. 1b shows, as $t \rightarrow \infty$, the PDF tends to become a dirac delta distribution. This is not surprising since the origin being the unique



a) With time, the PDF support shrinks and tends toward the asymptotic limit of impulse function.

b) Stacked PDF snapshots at the initial and five consecutive times, starting with a standard normal distribution.

Fig. 1 Evolution of the $\mathcal{N}(0, 1)$ initial PDF according to Eq. (15).

equilibrium of this dynamics, in the asymptotic limit, all probability mass gets in that sink. Thus, the support of the stationary distribution has Lebesgue measure zero.

2. 2-D Example

Next, consider a planar vector field

$$\dot{x} + x = -\frac{2y}{\log(x^2 + y^2)} \quad \dot{y} + y = \frac{2x}{\log(x^2 + y^2)} \quad (16)$$

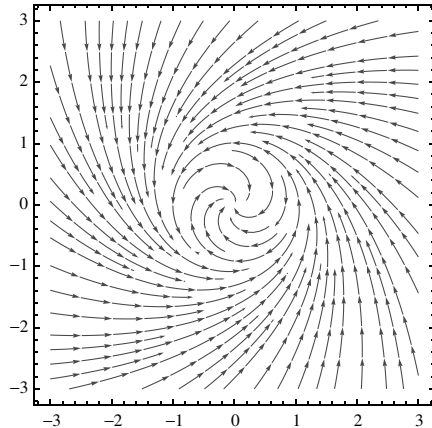
with given initial conditions $x(0) = x_0$ and $y(0) = y_0$. Looking at the form of the dynamics, we convert Eq. (16) from Cartesian to polar coordinates using the standard transformation $r\dot{r} = x\dot{x} + y\dot{y}$ and $\dot{\theta} = \frac{xy - yx}{x^2 + y^2}$ to obtain

$$\dot{r} = -r \quad \dot{\theta} = \frac{1}{\log r} \quad (17)$$

purely as a matter of working convenience. The initial conditions for Eq. (17) are $r_0 := r(0) = \sqrt{x_0^2 + y_0^2}$ and $\theta_0 := \theta(0) = \arctan \frac{y_0}{x_0}$. From the polar equations, it immediately follows that as $t \rightarrow \infty$, $r(t) \rightarrow 0$ and $|\theta(t)| \rightarrow \infty$ implying that the origin is a globally asymptotically stable spiral for this nonlinear system (Fig. 2). Notice, however, that a linear stability analysis predicts the origin to be a stable star. In fact, one can easily solve Eq. (17) to get the trajectory in closed form

$$r(r_0, t) = r_0 e^{-t}, \quad \theta(\theta_0, t) = \theta_0 + \log\left(\frac{\log r_0}{\log r_0 - t}\right) \quad (18)$$

which corroborates the asymptotic behavior mentioned above. Further, one can compute



$$\begin{aligned} \Psi &= \frac{\partial}{\partial r}(-r) + \frac{\partial}{\partial \theta}\left(\frac{1}{r}\right) = -1 \\ \Rightarrow \exp\left(-\int_0^t \Psi(r(\tau), \theta(\tau)) d\tau\right) &= e^t \end{aligned} \quad (19)$$

From Eq. (18), we also get

$$r_0(r, t) = re^t, \quad \theta_0(\theta, t) = \theta - \log\left(\frac{\log r + t}{\log r}\right) \quad (20)$$

Thus, Eqs. (19) and (20) result

$$\varphi(r, \theta, t) = \varphi_0(r_0, \theta_0)e^t = \varphi_0\left(re^t, \theta - \log\left(\frac{\log r + t}{\log r}\right)\right)e^t \quad (21)$$

If the initial conditions are sampled from a uniform distribution, the transient PDFs resemble the phase portrait of Fig. 2, converging toward a dirac delta at the origin. To examine the case for non-uniformly sampled initial conditions, an initial PDF is taken which has a high probability around $\theta = 0$ and is symmetric about the same. The polar plots of Fig. 3 shows the PDF contours at $t = 0, 0.2, 0.5, 1.0, 1.4$ and 2.0 , respectively, for the dynamics given by Eq. (16). It can be observed that the support of the transient PDFs shrink progressively and spirally converge toward the origin. The center (periphery) has high (low) probability.

Remark 1: The two simple examples given above illustrate how MOC solves the SLE. In MOC, the initial value problem (IVP) given by Eq. (8) is solved along the characteristics (which in case of SLE, are the integral curves or trajectories of the flow). Thus the integral in Eq. (9) is a path integral computed along each trajectory (see Fig. 4).

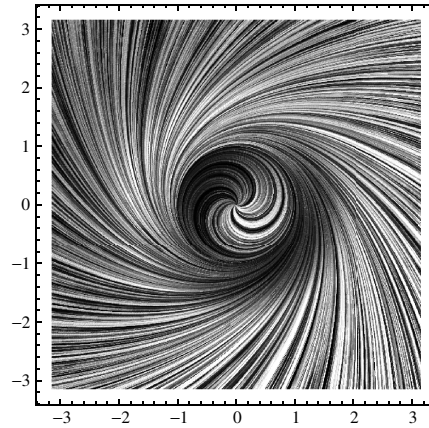


Fig. 2 Vector field (left) and an ensemble of trajectories in the phase space (right) for the nonlinear system given by Eq. (16).

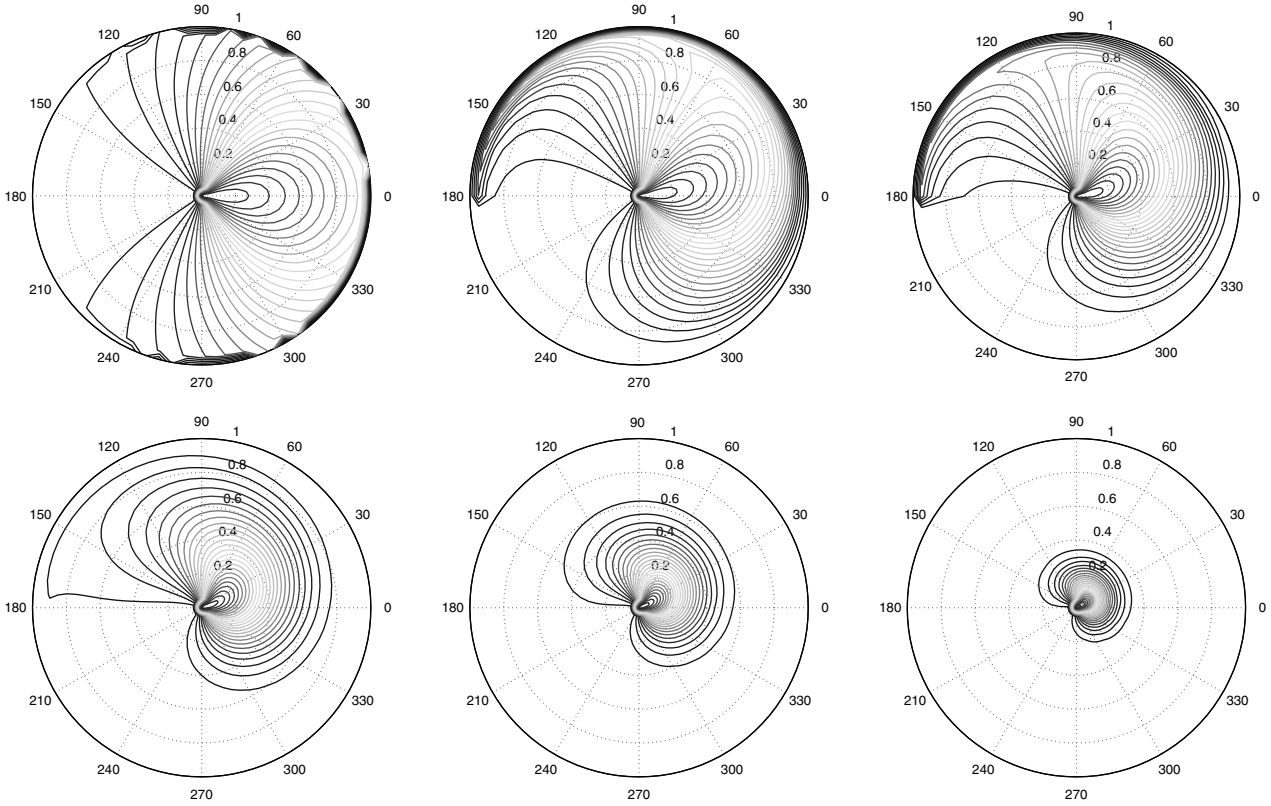


Fig. 3 The PDF contours computed from Eq. (21) at $t = 0, 0.2, 0.5, 1.0, 1.4$, and 2.0 , respectively.

To further clarify this, consider a divergence-free vector field. Then Eq. (8) tells us that the joint PDF remains constant as long as we are *riding* a particular trajectory. The value of this constant is different along a different trajectory. Thus, a volume-preserving flow, in general, does admit a spatio-temporally evolving PDF. For the same reason, in the above examples, initial condition was computed as a function of the current state and time to substitute for $\mathbf{X}(0)$ in $\varphi(\mathbf{X}(0), 0)$ [see Eqs. (14), (15), and (21)].

Remark 2: For the SLE, since the trajectories are same as the characteristic curves and trajectories cannot intersect (due to uniqueness), the solutions of the MOC are no where discontinuous. Further, notice that, to compute the inverse map of $\mathbf{x} = \mathbf{x}(\mathbf{x}_0, \mathbf{p}, t)$, of the form $\mathbf{x}_0 = \mathbf{x}_0(\mathbf{x}, \mathbf{p}, t)$, our earlier stated assumption of the continuity of \mathbf{x} on \mathbf{x}_0 , \mathbf{p} , and t , comes into play.

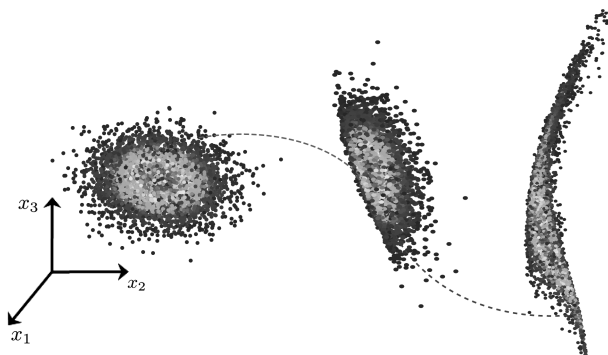


Fig. 4 In MOC based SLE method, along each sample trajectory, the probability weights are updated during dynamics propagation. In MC method, one tries to reconstruct a histogram to *approximate* such weight distribution, as a postprocessing step. So the main advantage of SLE compared with MC is the ability to update *exact* probability weights on the fly and hence, the samples are colored, so to speak, with the color-value being proportional to the value of the instantaneous joint PDF.

III. Nonlinear Flight Dynamics for Hypersonic Entry

In this paper, we will concentrate on applying the theoretical framework described above to the problem of hypersonic EDL modeled through Vinh's equations [33]. We will work with two different versions of the model, a three state model where the dynamics is assumed to be purely longitudinal, and a more general six-state model with lateral-longitudinal coupling. Both these models describe the trajectory of the center-of-mass of the spacecraft entering into the Mars atmosphere.

A. Three-State Model

Assuming the entire trajectory is contained in the longitudinal plane, one can write the following nondimensionalized three-state (h, V, γ) model for nonrotating spherical Mars with zero bank angle flight.

$$\dot{h} = V \sin \gamma \quad (22a)$$

$$\dot{V} = -\frac{\rho R_0}{2B_c} V^2 - \frac{g R_0}{v_c^2} \sin \gamma \quad (22b)$$

$$\dot{\gamma} = \frac{\rho R_0 C_L}{2B_c C_D} V + \frac{g R_0}{v_c^2} \cos \gamma \left(\frac{V}{1+h} - \frac{1}{V} \right) \quad (22c)$$

Here the model for Martian atmospheric density variation [34] is taken as

$$\rho = \rho_0 \exp \left(\frac{h_2 - h R_0}{h_1} \right) \quad (23)$$

where $h_2 = 20$ km and $h_1 = 9.8$ km. The mean equatorial radius of Mars will be taken as $R_0 = 3397$ km.

B. Six-State Model

Here we present the more general form of Vinh's equations, which is a nondimensionalized six-state $(h, \zeta, \lambda, V, \gamma, \chi)$ model. This

model takes the self-rotation rate Ω of the planet and the bank angle σ into account.

$$\dot{h} = V \sin \gamma \quad (24a)$$

$$\dot{\zeta} = \frac{V \cos \gamma \sin \chi}{(1 + h)} \quad (24b)$$

$$\dot{\lambda} = \frac{V \cos \gamma \cos \chi}{(1 + h) \cos \zeta} \quad (24c)$$

$$\begin{aligned} \dot{V} = & -\frac{\rho R_0}{2B_c} V^2 - \frac{g R_0}{v_c^2} \sin \gamma \\ & + \frac{R_0^2 \Omega^2}{v_c^2} (1 + h) \cos \zeta (\sin \gamma \cos \zeta - \cos \gamma \sin \zeta \sin \chi) \end{aligned} \quad (24d)$$

$$\dot{\gamma} = \frac{\rho R_0 C_L}{2B_c C_D} V \cos \sigma + \frac{g R_0}{v_c^2} \cos \gamma \left(\frac{V}{1 + h} - \frac{1}{V} \right) \quad (24e)$$

$$\begin{aligned} \dot{\chi} = & \frac{\rho R_0 C_L}{2B_c C_D} \frac{V \sin \sigma}{\cos \gamma} - \frac{V \cos \gamma}{(1 + h)} \tan \zeta \cos \chi \\ & + \frac{2R_0 \Omega}{v_c} (\tan \gamma \cos \zeta \sin \chi - \sin \zeta) \\ & - \frac{R_0^2 \Omega^2}{v_c^2} \frac{(1 + h)}{V \cos \gamma} \sin \zeta \cos \zeta \cos \chi \end{aligned} \quad (24f)$$

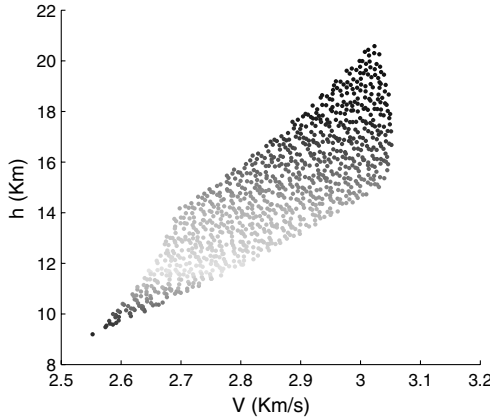
Ω was calculated from the rotational time period of Mars, which is 24 h, 39 min, and 35.24 s. The density variation is taken identical to the three-state model.

IV. Application of SLE to Some Specific Cases

Before solving SLE for the models described in the preceding section, we will examine certain restricted cases of the same. Since the three and six-state models, in general, require numerical solution for the PDF, considering some specific cases will give us some physical understanding of the problem. Many case studies of this nature can be found in [14] (see Ch. 7).

A. Horizontal Flight

For horizontal flight, $\gamma \approx 0$ and $h = \text{constant}$. Therefore, only the second equation remains to be considered in Eq. (18), which becomes



a) Scatterplot at $t = 19.13$ sec with 5% uniform initial condition uncertainties in h_0 and V_0

$$\begin{aligned} \dot{V} &= -\frac{\rho R_0}{2B_c} V^2 \\ &\Rightarrow \int_{V_0}^V \frac{dV}{V^2} = -\frac{\rho R_0}{2B_c} \int_0^t dt \quad [\text{since } h \text{ is constant, so is } \rho] \\ &\Rightarrow V = \frac{V_0}{1 + \frac{\rho R_0}{2B_c} V_0 t} \end{aligned} \quad (25)$$

which implies that V decreases monotonically with time. In this case, $\varphi(V, t) = \varphi_0(V_0) \exp(-\int_0^t \Psi(V(\tau)) d\tau)$, where $\Psi(V) = \frac{\rho R_0}{B_c} V$. Therefore

$$\begin{aligned} \varphi(V, t) &= \varphi_0(V_0) \left[1 + \frac{\rho R_0}{2B_c} V_0 t \right]^2 = \varphi_0(V_0) \left(\frac{V_0}{V} \right)^2 \\ &= \varphi_0 \left(\frac{V}{1 - \frac{\rho R_0}{2B_c} V t} \right) \frac{1}{(1 - \frac{\rho R_0}{2B_c} V t)^2} \end{aligned} \quad (26)$$

Thus, given an initial PDF describing the initial condition uncertainty, Eq. (26) provides an algebraic expression for determining the PDF at any current time and velocity.

B. Vertical Flight

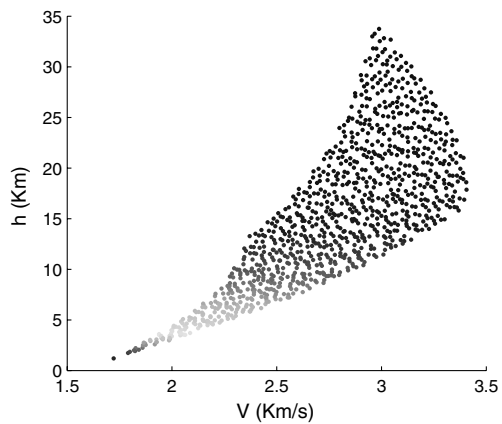
This special case concerns the vertical descent ($\gamma = -\frac{\pi}{2}$) in a nonlifting trajectory. Consequently, we eliminate Eq. (22c) as all terms in it are identically zero. Hence, we are left with Eqs.(22a), (22b), and (23). Substituting ρ in Eq. (22b) as a function of h , we get two first-order coupled nonlinear ODEs in h and V , shown below

$$\dot{h} = -V \quad (27a)$$

$$\dot{V} = -K_1 V^2 e^{-\beta h} + K_2 \quad (27b)$$

with $K_1 = \frac{\rho_0 R_0}{2B_c} e^{h_0/h_1}$, $\beta = \frac{R_0}{h_1}$ and $K_2 = \frac{g R_0}{v_c^2}$. With $\Psi = -2K_1 V e^{-\beta h}$, the SLE needs to be solved numerically along with the above dynamics.

With nominal initial altitude $h_0 = 80$ km and nominal initial velocity $V_0 = 3.5$ km/s, and assuming 5% uniform dispersion in both h_0 and V_0 , the SLE was solved numerically. The simulation was repeated for 15% uniform dispersion in both h_0 and V_0 . In both the cases, 1000 samples were taken to represent the trajectory ensemble. Figure 5 shows the color-coded scatter plots at $t = 19.13$ seconds in the hV plane with the color-value being proportional to the value of the bivariate joint PDF at that instant. Notice that, a larger dispersion in the initial conditions results in more spread in the point cloud at the same instant of time.



b) Scatterplot at $t = 19.13$ sec with 15% uniform initial condition uncertainties in h_0 and V_0

Fig. 5 Scatterplot snapshots for uncertainty evolution of systems (27a) and (27b) with uniform dispersions in the initial conditions.

V. Numerical Simulations

In this section, the numerical simulation set up is described for solving the SLE for the three- and six-state models described in Sec. III. The simulation framework is provided in detail followed by results and discussions.

A. Simulation Setup

The nominal initial conditions were taken to be $h_0 = 80$ km, $\zeta_0 = 24.01^\circ\text{N}$, $\lambda_0 = 341.03^\circ\text{E}$, $V_0 = 3.5$ km/s, $\gamma_0 = -2^\circ$ and $X_0 = 0.0573^\circ$. The nominal values of the parameters were taken as $B_c = 72.8$ kg/m², $\rho_0 = 0.0019$ kg/m³ and $\frac{C_L}{C_D} = 0.3$. Because the models described in Sec. III are nondimensionalized, numerical integration was performed in nondimensional time $\tilde{t} = 0$ to 0.7 with the nondimensional step-size of $\Delta\tilde{t} = 0.01$. One can easily convert it back to the physical time by multiplying the nondimensional time with a factor $\frac{R_0}{v_e}$. In this paper, results are presented for two kinds of initial uncertainties, viz. 5% uniform dispersion in each variable and Gaussian dispersion about the nominals with 10% variance along each dimension.

B. Simulation Framework

The simulation framework comprises of three main modules as described below.

1. Sampling Initial Distribution

The initial uncertainties are specified by an initial joint PDF. Once the initial joint PDF is known, one needs to generate a prespecified number of samples such that they best represent that joint PDF. For the case of uniform initial distribution, one may do a grid-based discretization or for high dimensions, opt for a pseudorandom number generator using low-discrepancy sequences like *Halton sequence* [13] to avoid the curse of dimensionality. Some preliminary comparative simulation results along these lines were reported in [35]. In this paper, samples from uniform initial PDF were generated using multidimensional Halton sequence. For nonuniform initial PDFs, one need to use probability integral transform (e.g., Box–Muller transform in case of normal distribution) methods [36]. However, one must resort to the Markov Chain MC [37–39] (MCMC) techniques to achieve better computational performance for sampling any general initial PDF in high dimensions [40].

2. Uncertainty Propagation

The samples from the initial uncertainty polytope are propagated according to the dynamics given in Sec. III and the SLE is solved at each time step. Four libraries are required to achieve this. The dynamics library specifies the nonlinear model and the atmosphere model is provided in a separate library, which is used by the dynamics. Another library does gradient computation (analytically for the present case or using finite differencing for a black box model) needed to solve the SLE. A fourth-order Runge–Kutta (RK4) based integrator was used to propagate the dynamics and for solving the SLE. All results reported below are from the MATLAB® implementation using variable step-size `ode45` integrator.

3. Postprocessing of the Joint PDF Data

As the samples from the initial PDF are propagated according to dynamics, the joint PDF at any given time is represented by the instantaneous distribution of those evolved samples. Because of the nonlinear dynamics, such a distribution, in general, is a scattered data set residing over the extended state space. These evolved joint PDFs are required to compute the marginal distributions that correspond to those typically used in EDL analysis. For doing this, one needs to isolate a snapshot of interest and integrate out the dimensions other than whose marginal is sought. In Sec. II.A, we briefly touched upon the fact that because of dynamics, the domain or the support of the joint PDF deforms with time and the integration for marginal computation needs to be carried out over few dimensions of this

instantaneous domain. This brings forth the problem of integration over high-dimensional scattered data.

One way to tackle this problem is to interpolate these scattered data, which itself is numerically challenging. We mention here that since the joint PDF values were computed directly by solving SLE, it is an interpolation problem as opposed to function approximation. Alternatively, one may attempt the numerical integration without interpolation. For this, one can sprinkle a new set of Halton points (preferably more than the number of samples) inside the bounding box of this static/time-frozen data and then use these newly sprinkled points as the quadrature points to carry out quasi-MC (QMC) integration [13] (see Ch. 2). The computational cost associated with this approach comes from the evaluation of the joint PDF values at this new set of points, which can be determined by first back-integrating the dynamics and then forward integrating the SLE for these quadrature points.

Notice, however, that for computing marginals from MC simulations, one takes a frequentist approach and counts samples in the bins lying on the requisite slices. Because we are interested to compare the SLE derived marginals with those obtained from MC, a similar (and computationally less heavy than described above) method can be employed to approximate the marginals from SLE. In the PF-derived SLE method, since one has a probability weight associated with each sample, one can do a binning similar to MC histograms. Only this time, instead of counting the number of samples in each bin, the bin weight can be assigned as the average of the joint PDF values of the samples in that bin (see Fig. 6). In both cases, the individual bin weights need to be normalized with respect to the bin size and total probability weight. All marginals of PF-derived SLE method presented here, are computed in this fashion.

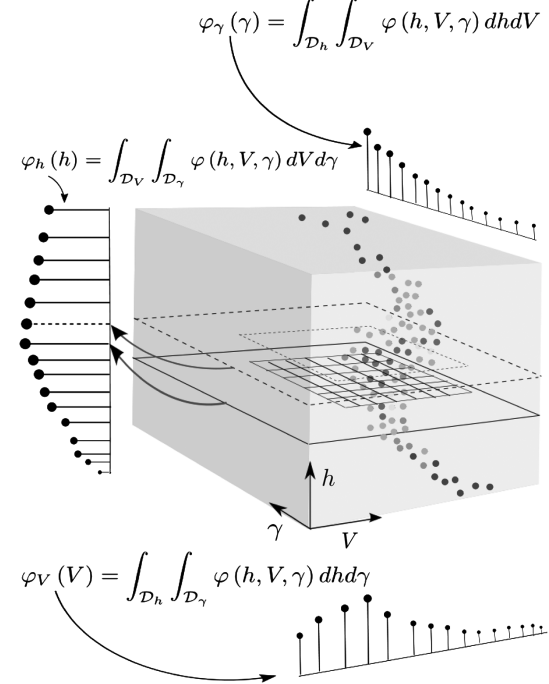


Fig. 6 A schematic for computing marginals from scattered instantaneous joint PDF data. For example, after solving the SLE for three-state Vinh's equations with initial condition uncertainties, to compute univariate marginal in h , one would take $V\gamma$ slices at different sample levels of altitude. At each such slice (the one with solid edges), one can average out the V and γ directions using the joint PDF values as explained in Sec. V.B.3 and obtain a scalar value. One would then shift this slice at the next h sample level (dotted slice) and repeat the exercise. This results the h -marginal vector $\varphi_h(h)$ as shown. By taking slices in other orthogonal directions, one can similarly get $\varphi_V(V)$ and $\varphi_\gamma(\gamma)$. The idea can be easily extended to compute higher dimensional marginals.

C. Results and Discussion

For the three-state model, it is possible to visualize the joint PDF using three dimensional color-coded scatter plots similar to Fig. 5. Such plots are shown in Fig. 7 for 1000 samples at $\tilde{t} = 0.05, 0.20, 0.30$, and 0.50 with both uniform (top row) and Gaussian (bottom row) initial condition uncertainties. It can be observed that at $\tilde{t} = 0.05$, the joint PDFs are slightly perturbed from the respective initials. As time progresses, the probability mass accumulates near zero altitude and zero velocity and the flight-path angle (FPA) assumes a steep value. This is in agreement with the physical intuition as the vehicle, with high probability, slows down through the lower part of the atmosphere.

Starting from the uniform initial joint PDF, the evolution of the univariate and bivariate marginals for the three-state Vinh's equations, are shown in Fig. 8. The same for the Gaussian initial PDF are plotted in Fig. 9. The univariate MC (dashed) and PF (solid) PDFs are in good match. The bivariate marginals show the general trend that PF-derived marginals (bottom row) capture the concentration of the probability mass well (by virtue of the probability weights obtained by solving SLE) while the MC bivariate marginals (top row) tend to smear it out (because of the histogram approximation). This can be seen, for example, in $V\gamma$ bivariate plots. Similar trends can be observed for the six-state model. For brevity, in Fig. 10, we only show the snapshot of univariate PDFs at $\tilde{t} = 0.30$ for the six-state model with uniform initial PDF.

The simulation results shown above bears testimony to the fact that with same number of simulations, PF operator based approach can better resolve the PDF compared with MC method. This is not surprising since the former assigns explicit probability weights computed by solving the SLE while the latter tries to construct a PDF using crude histogram approximation. The success of the latter (in terms of good approximation of the PDF) is heavily dependent on the number of sample trajectories being evolved. Hence, SLE-based PF methods can be computationally attractive over MC, particularly in high-dimensional nonlinear problems like spacecraft EDL, as it evolves less number of high initial probability samples to achieve an accurate resolution of the PDF.

To quantify the closeness of the MC and PF based marginal PDFs shown before, two information-theoretic quantities were used, viz. Kullback–Leibler (KL) divergence Δ_{KL} and Hellinger distance Δ_{HL} . The KL divergence measures the distance between two PDFs $\mathcal{P}(x)$ and $\mathcal{Q}(x)$, and is defined as

$$\Delta_{KL}(\mathcal{P} \parallel \mathcal{Q}) := \int_{-\infty}^{+\infty} \mathcal{P}(x) \log \frac{\mathcal{P}(x)}{\mathcal{Q}(x)} dx \quad (28)$$

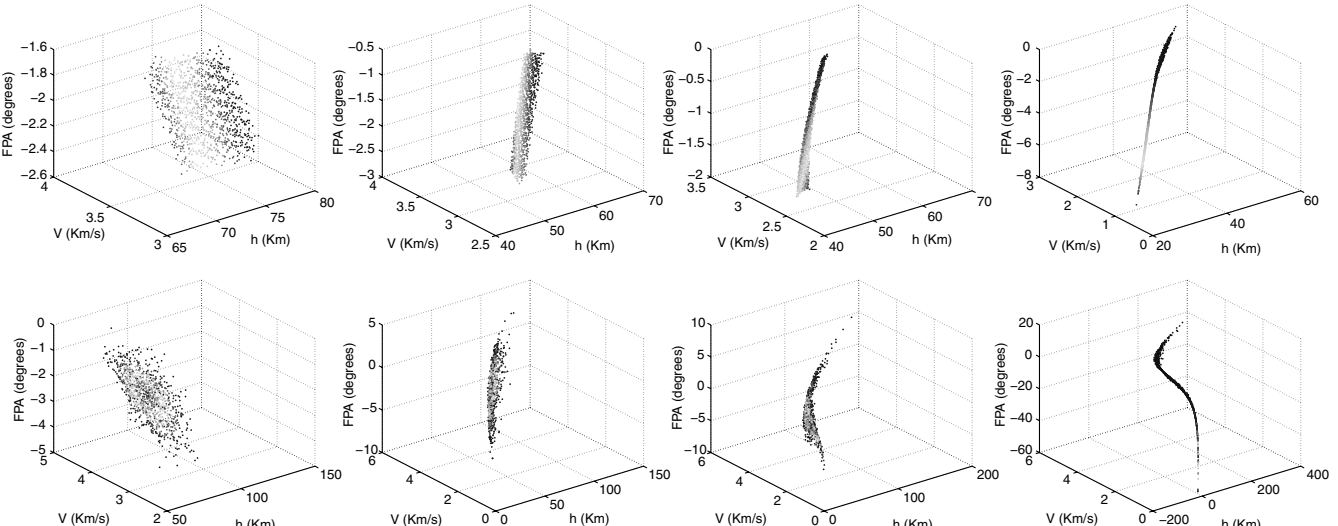


Fig. 7 Scatter plots of the joint PDF with three dimensional support (h, V, γ) at $\tilde{t} = 0.05, 0.20, 0.30$, and 0.50 , respectively. Columns show different times, rows signify different initial PDFs (uniform at top and Gaussian at bottom row).

It can be interpreted as the relative entropy between two PDFs and is a pseudometric (nonsymmetric and does not obey triangle inequality). A similar quantity, Hellinger distance, is defined as

$$\Delta_{HL}^2(\mathcal{P} \parallel \mathcal{Q}) := \frac{1}{2} \int_{-\infty}^{+\infty} (\sqrt{\mathcal{P}(x)} - \sqrt{\mathcal{Q}(x)})^2 dx \quad (29)$$

and it does obey the triangle inequality. Further, since Hellinger distance lies between 0 and 1, it can be interpreted as the percentage distance between two densities. In Fig. 11, KL divergence and Hellinger distance between the respective univariate marginals of the three-state Vinh's equations are plotted for $\tilde{t} = 0.30$ for the case with uniform initial PDF. The superscripts denote the respective variables. The PF marginals are taken as the reference densities. We observe that MC marginals are in close match with the PF ones at this instant. However, as the PDF evolves further, the difference between the histogram-based MC and SLE-based PF marginals become more prominent, as was qualitatively observed in Fig. 8. The two information-theoretic metrics provide a quantitative measure of the same. Figure 12 shows the variation of these information metrics with sample size for $\tilde{t} = 0.50$. Notice the increase in the ordinate values by at least an order of magnitude, compared with the same in Fig. 11. The exercise can be repeated for various time instances to get an idea of the computational performance.

VI. Further Statistical Analysis

In this section, we will demonstrate few case studies pertaining to EDL specific analysis in the SLE framework.

A. Case I: Tracking Uncertainty

It is of interest to compute the probability that the flight-path angle (FPA) will be within a specified interval, i.e., $\gamma_{\min} \leq \gamma \leq \gamma_{\max}$. This problem is important in the context of tracking the spacecraft by a space-based antenna. Univariate FPA marginals (like those shown in Figs. 8–10) can be computed at different times to calculate the tracking probabilities. Such information can be crucial from mission design perspective.

B. Case II: Landing Footprint Uncertainty

Computing the landing footprint uncertainty has been one of the key aspects of EDL analysis. Important decisions like landing risk evaluation and trajectory correction maneuver (TCM) design depend on it. A list of factors contributing toward landing footprint uncertainty, can be found in [9]. Almost all EDL analysis has been

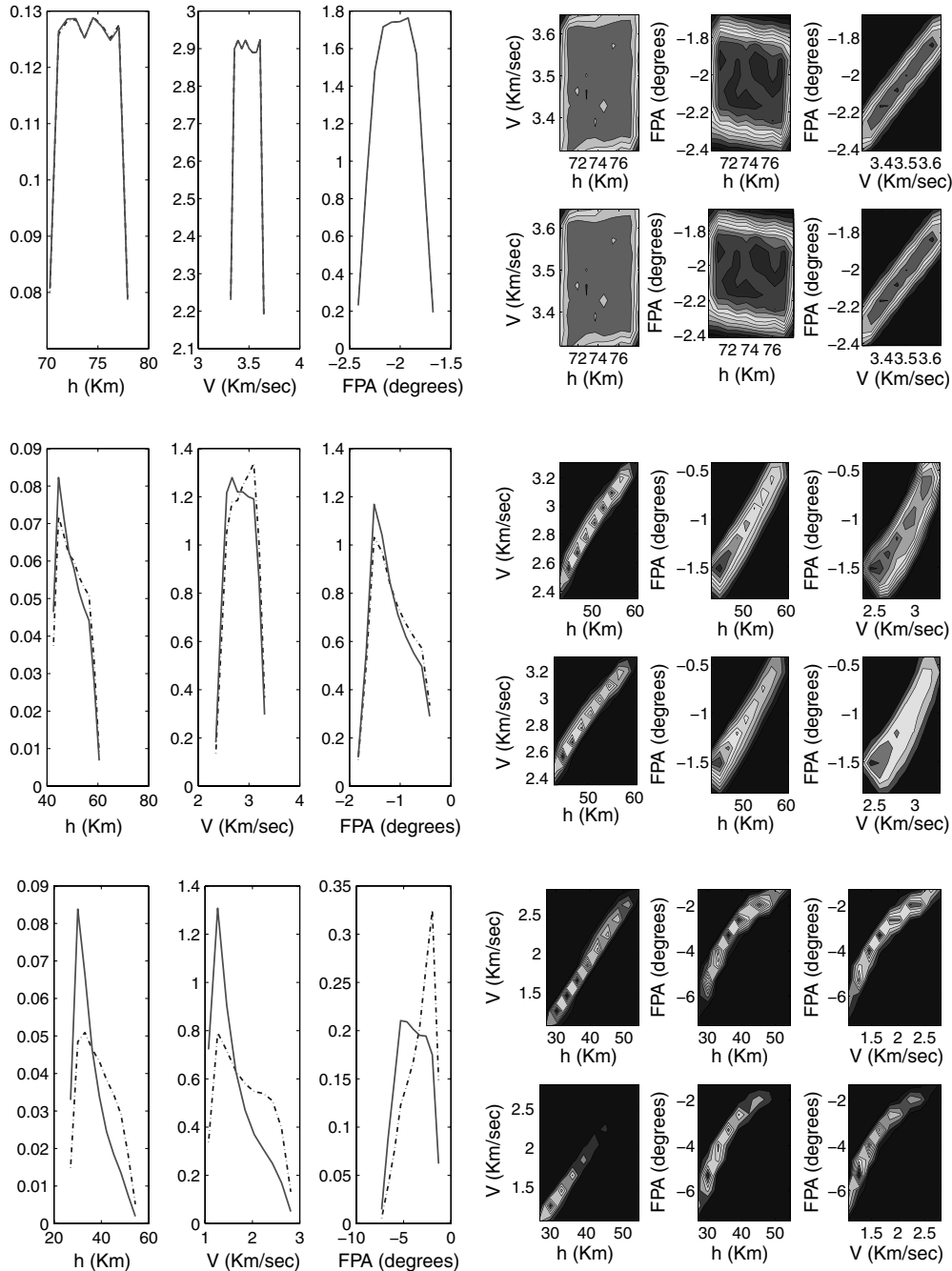


Fig. 8 The univariate and bivariate marginals for the case of uniform initial condition uncertainty at $\tilde{t} = 0.05, 0.30$ and 0.50 , respectively. The simulation is for three-state Vinh's equations with 5000 samples. For univariate marginals, PF results are in solid and MC results are in dashed. For bivariate marginals, PF results are in the bottom row and MC results are in the top row.

based on evolving a bivariate Gaussian in latitude and longitude and thereby characterizing a 3σ landing ellipse representing the landing footprint uncertainty. Historically, the landing ellipses have spanned hundreds of kilometers (see Fig. 13).

However, depending on the initial uncertainty and system dynamics, the latitude-longitude bivariate marginal can be far from Gaussian, resulting the 3σ estimates unrealistic. On the other hand, computing this marginal using MC method is not only computationally expensive but can be inaccurate, for reasons discussed in Sec. V.C. Figure 14 compares the latitude-longitude ($\zeta \lambda$) bivariate marginal at the final time, computed for the six-state model using MC (left) and SLE-based PF (right) method. Notice that, the SLE-based PF method (right in Fig. 14) predicts the landing footprint to be at approximately 377 deg east and 21.3 deg north, with maximum probability and a very small dispersion around it. It ascertains that the landing probability everywhere else is zero. In

contrast, MC method (left in Fig. 14) can at best predict a high probability around 357–381 deg east and 20.5–21.4 deg north and is unable to do any further refinement of the landing footprint uncertainty. Not surprisingly, such huge MC dispersion in latitude-longitude results 3σ landing ellipse spanning hundreds of kilometers. It is evident that SLE-based PF method outperforms MC.

Looking at such dramatic localization of uncertainty computed through SLE (Fig. 14), one should not get confused by thinking that SLE underpredicts uncertainties. SLE simply computes *exact* probability density values whereas MC *approximately* reconstructs these values through histogram. Based on the approximation parameters (e.g., number of bins, overlapping or nonoverlapping bins, equal or unequal bin-size, etc.), the MC method, as a piecewise constant approximation algorithm, may underpredict or overpredict uncertainty. In either case, SLE stands superior as exact value, irrespective of the relative size of the PDF support.

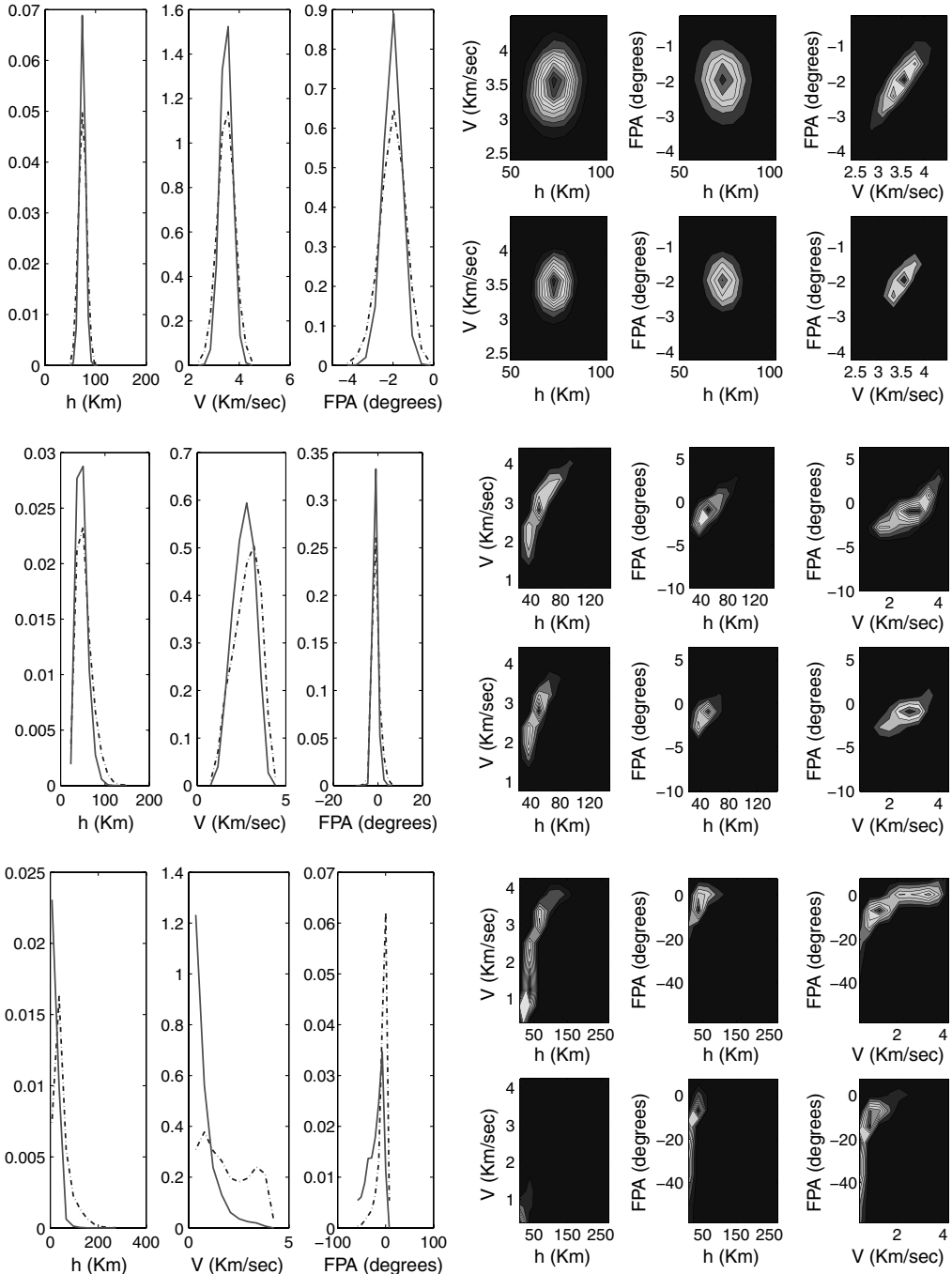


Fig. 9 The univariate and bivariate marginals for the case of Gaussian initial condition uncertainty at $\tilde{t} = 0.05, 0.30$ and 0.50 , respectively. The simulation is for three-state Vinh's equations with 5000 samples. Conventions for the MC and PF plots are same as in the previous figure.

C. Case III: Heating Rate Uncertainty

It is of interest to compute the univariate density of heating rate \dot{Q} (j/s) given by

$$\begin{aligned}\dot{Q} &= \frac{1}{4} C_f \rho V^3 S = \frac{1}{4} C_f \rho_0 \exp\left(\frac{h_2 - h R_0}{h_1}\right) V^3 S \\ &= \alpha V^3 e^{-\beta h} \triangleq \phi(V, h) \quad (\text{say})\end{aligned}$$

where $\alpha = \frac{1}{4} C_f \rho_0 S e^{\frac{h_2}{h_1}}$ and $\beta = \frac{R_0}{h_1}$. Here C_f refers to the skin-friction coefficient of the exterior surface area of the entry capsule. Let us introduce an auxiliary random variable $\zeta = V \triangleq \psi(V, h)$. The functions ϕ and ψ define a mapping $(V, h) \mapsto (\dot{Q}, \zeta)$. Jacobian (and its determinant) of this transformation can be calculated as

$$J = \begin{bmatrix} \frac{\partial \phi}{\partial V} & \frac{\partial \phi}{\partial h} \\ \frac{\partial \psi^{-1}}{\partial V} & \frac{\partial \psi^{-1}}{\partial h} \end{bmatrix} = \begin{bmatrix} 3\alpha V^2 e^{-\beta h} & -\alpha \beta V^3 e^{-\beta h} \\ 1 & 0 \end{bmatrix} \Rightarrow \det(J) = \alpha \beta V^3 e^{-\beta h}. \quad (30)$$

Root of the *inverse mapping* is found to be

$$(V^*, h^*) = \left(\zeta, \frac{1}{\beta} \log\left(\frac{\alpha \zeta^3}{\dot{Q}}\right) \right) \quad (31)$$

From the equation before Eq. (31), one can evaluate the determinant of the Jacobian at the root of the inverse mapping given by Eq. (31) as

$$\det(J^*) = \alpha \beta \zeta^3 \frac{\dot{Q}}{\alpha \zeta^3} = \beta \dot{Q} \quad (32)$$

Because $\alpha, \beta, V > 0$, it is easy to verify that the mapping $(V, h) \mapsto (\dot{Q}, \zeta)$ defined by the functions ϕ and ψ , is bijective.

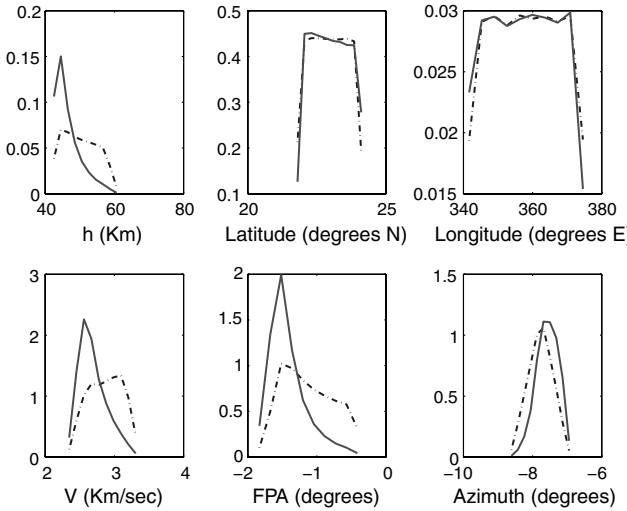


Fig. 10 The univariate marginals for the case of uniform initial condition uncertainty at $\tilde{t} = 0.30$. The simulation is for 6 state Vinh's equations with 10,000 samples. PF results are in solid and MC results are in dashed.

Consequently, the joint density in the transformed variables (ζ, \dot{Q}) is given by

$$\eta(\zeta, \dot{Q}) = \frac{\xi(V^*, h^*)}{|\det(J^*)|} \quad (33)$$

where $\xi(.,.)$ is the bivariate marginal in V and h . Further, $\eta(\dot{Q}) = \int_0^\infty \eta(\zeta, \dot{Q}) d\zeta$. Thus, from Eqs. (31–33), we have

$$\eta(\dot{Q}) = \int_0^\infty \frac{1}{\beta \dot{Q}} \xi\left(\zeta, \frac{1}{\beta} \log\left(\frac{\alpha \zeta^3}{\dot{Q}}\right)\right) d\zeta \quad (34)$$

Figure 15 shows the univariate PDFs for \dot{Q} per unit area (in W/cm^2) for the three-state model (left) and for the six-state model (right), both with uniform initial condition uncertainty. The solid lines show the SLE result and the dashed lines show the MC based histogram approximation.

D. Case IV: Chute Deployment Uncertainty

Quantification of uncertainty for the purpose of chute deployment is of growing interest as future Mars missions are expected to deploy at higher Mach numbers [1]. It is important to schedule the deployment in an Mach number M and dynamic pressure q regime

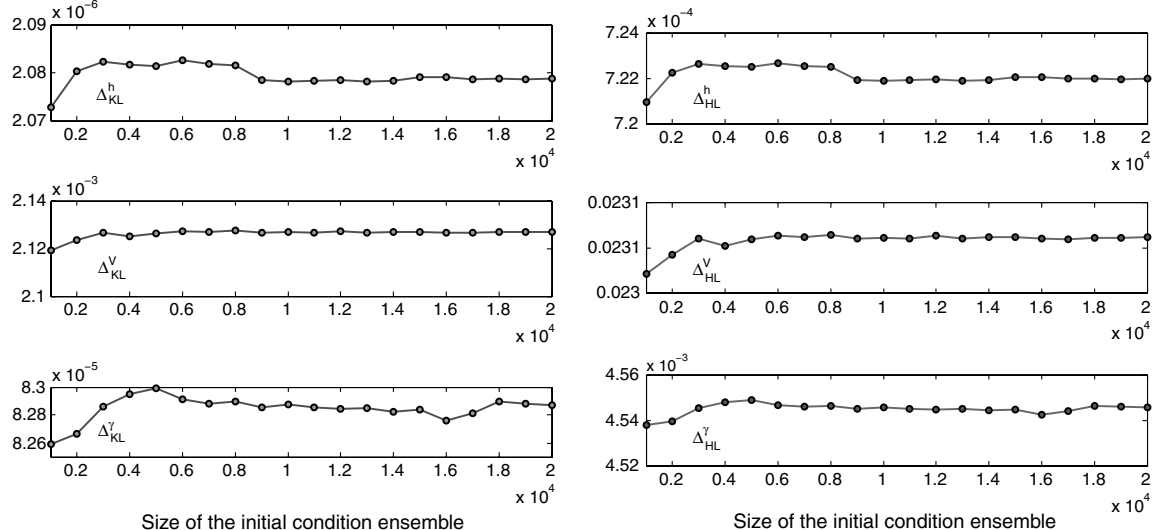


Fig. 11 Variation of the KL divergence (left) and Hellinger distance (right) with number of samples. Snapshots are compared at $\tilde{t} = 0.30$.

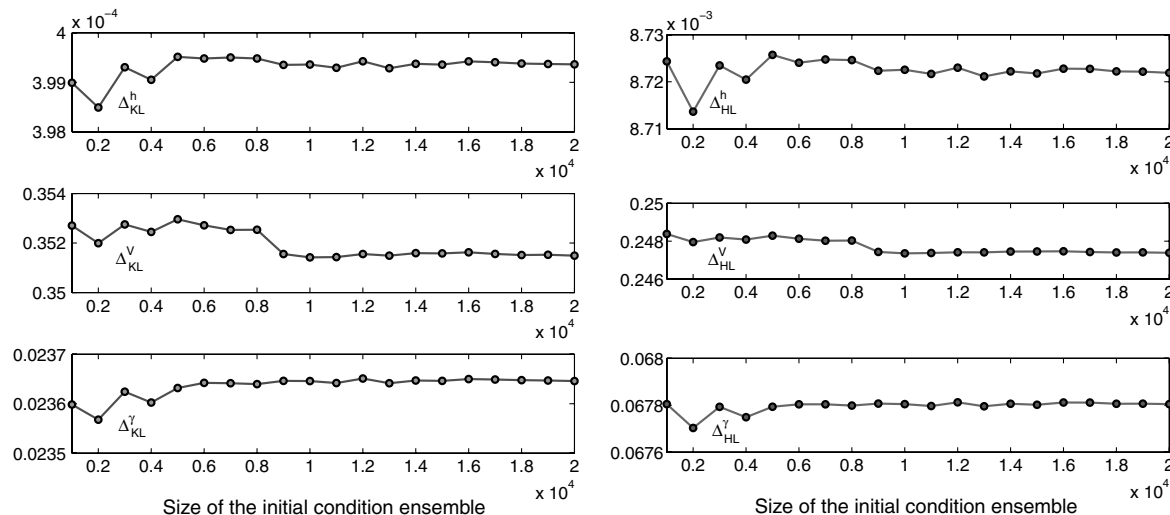


Fig. 12 Variation of the KL divergence (left) and Hellinger distance (right) with number of samples at the instant $\tilde{t} = 0.50$.

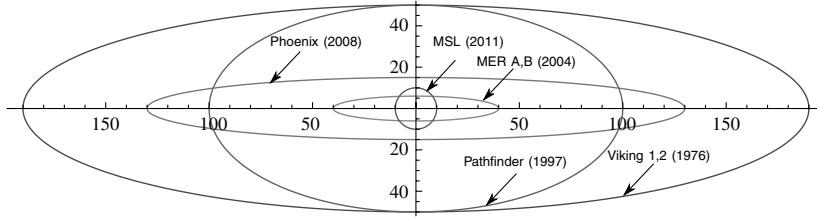


Fig. 13 Schematic comparison of landing footprints of Mars missions. To make a comparison between their sizes, all ellipses are drawn with the same center and same orientation. The scale on each axis is in Km (data taken from [1]). The ellipse for the upcoming MSL mission is anticipated.

such that the parachute can bear the stress and provide the requisite aerodynamic deceleration performance. The question considered here is whether the bivariate density in M and q is contained in a prespecified M - q box. If significant amount of probability mass lies outside this M - q box at the moment of chute deployment, then it would be probabilistically unsafe to deploy the supersonic parachute at that moment. From a mission design perspective, one can repeat this analysis to find the best time to deploy the chute for robust performance. Historically, for DGB parachutes, the Viking qualification program has guided the *design M-q box dimension* to be $M = 1.1\text{--}2.2$ and $q = 239\text{--}850 \text{ Pa}$ [12].

To characterize the Mach- q uncertainty, one needs to find the transformed bivariate density $\eta(M, q)$ from the bivariate marginal density $\xi(V, h)$. The mapping considered here is $(V, h) \mapsto (M, q)$ and is defined by

$$M = \frac{V}{\sqrt{\gamma R_* T(h)}} \triangleq \phi(V, h) \quad (35)$$

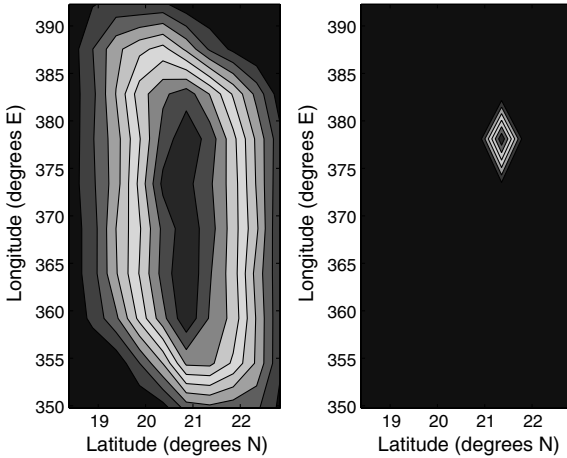


Fig. 14 Comparison of the latitude-longitude (ξ, λ) bivariate marginal PDF at the final time, from MC (left) and SLE-based PF (right) method.

$$q = \frac{1}{2} \rho V^2 = \frac{1}{2} \rho_0 \exp\left(\frac{h_2 - hR_0}{h_1}\right) V^2 = \Lambda V^2 e^{-\beta h} \triangleq \psi(V, h) \quad (36)$$

where $\Lambda = \frac{1}{2} \rho_0 e^{\frac{h_2}{h_1}}$ and $\beta = \frac{R_0}{h_1}$, as defined in Case III. Here γ is the ratio of specific heats and R_* is the difference between them (assuming ideal gas). As before, one must find the Jacobian of this transformation and compute the determinant as

$$J = \begin{bmatrix} \frac{\partial \phi}{\partial V} & \frac{\partial \phi}{\partial h} \\ \frac{\partial \psi}{\partial V} & \frac{\partial \psi}{\partial h} \end{bmatrix} = \begin{bmatrix} \frac{1}{\sqrt{\gamma R_* T(h)}} & -\frac{V}{2\sqrt{\gamma R_* (T(h))^{3/2}}} \frac{dT}{dh} \\ 2\Lambda V e^{-\beta h} & -\Lambda \beta V^2 e^{-\beta h} \end{bmatrix} \quad (37)$$

$$\Rightarrow \det(J) = \frac{\Lambda V^2 e^{-\beta h}}{\sqrt{\gamma R_* T(h)}} \left[\frac{1}{T(h)} \frac{dT}{dh} - \beta \right] \quad (38)$$

Now one can proceed to compute the roots of the inverse mapping, i.e., h and V as functions of M and q . To do this, one can substitute $V^2 = M^2 \gamma R_* T(h)$ [from (28)] in Eq. (36) to get

$$T(h) e^{-\beta h} = \frac{q}{\Lambda M^2 \gamma R_*} = C \quad (\text{say}) \quad (39)$$

At this point, let us assume $T(h) = -A - Bh$ for Mars atmosphere. Then Eq. (39) leads to

$$A + Bh + Ce^{\beta h} = 0 \quad (40)$$

This transcendental equation in h can be solved in closed form in terms of the *Lambert W function*

$$h^* = -\frac{A}{B} - \frac{1}{\beta} W_0\left(\frac{C\beta}{B} e^{-\frac{A\beta}{B}}\right) \quad (41)$$

provided $B\beta \neq 0$, which holds true for the case under consideration. Notice that, since $\beta, B, C > 0$, the associated Lambert *W* function is single valued (zeroth branch (usually referred as the principal branch) of *W*, denoted as W_0) and consequently Eq. (41) is the unique solution of Eq. (40). It should be emphasized here that the constant A is a negative scalar. This is because the temperature is given by T (in

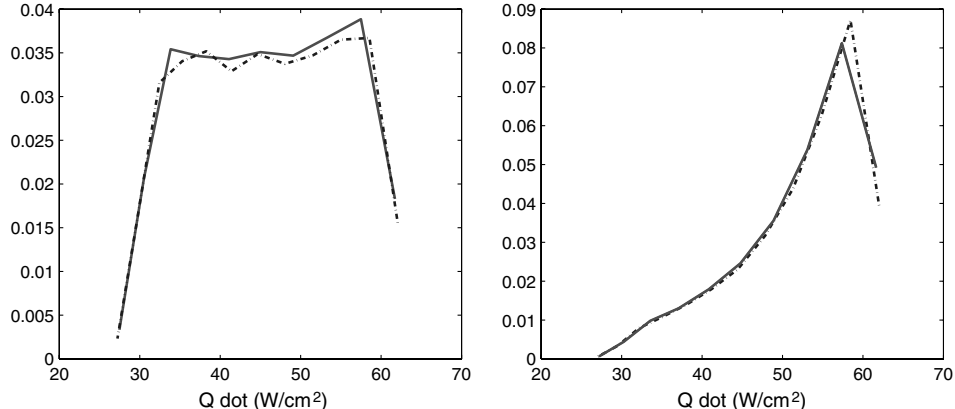


Fig. 15 Heating rate PDF snapshot at $\tilde{t} = 0.30$ for the three-state model with 5000 samples (left) and for the six-state model with 10,000 samples, both with uniform IC uncertainty (right). Solid lines show SLE derived PDFs, dashed lines show MC based histogram approximation.

$^{\circ}\text{C} = -a - Bh$ where $273.15 > a > 0$, $B > 0$ and h is in meters. Hence, the absolute temperature T (in Kelvin) $= -a - Bh + 273.15 = -A - Bh$ with $A = a - 273.15 < 0$. This will avoid any confusion about the sign of h^* .

Substituting Eq. (41) in Eq. (28), one can obtain

$$V^* = M \sqrt{\gamma R_* T(h^*)} = M \sqrt{\frac{\gamma R_* B}{\beta}} W_0 \left(\frac{C\beta}{B} e^{-\frac{A\beta}{B}} \right) \quad (42)$$

Thus the root for the inverse mapping is the doublet (V^*, h^*) given by Eqs. (41) and (42), where it is reemphasized that C is a function of both M and q , as given in Eq. (39).

Combining Eqs. (38), (41), and (42) and noting that $T(h^*) = \frac{B}{\beta} W_0 \left(\frac{C\beta}{B} e^{-\frac{A\beta}{B}} \right)$, one can derive

$$|\det(J^*)| = \Lambda M^2 e^{\frac{A\beta}{B}} \sqrt{\beta \gamma R_* B} \left(\frac{\left(\frac{C\beta}{B} e^{-\frac{A\beta}{B}} \right) + e^{W_0 \left(\frac{C\beta}{B} e^{-\frac{A\beta}{B}} \right)}}{\sqrt{W_0 \left(\frac{C\beta}{B} e^{-\frac{A\beta}{B}} \right)}} \right) \quad (43)$$

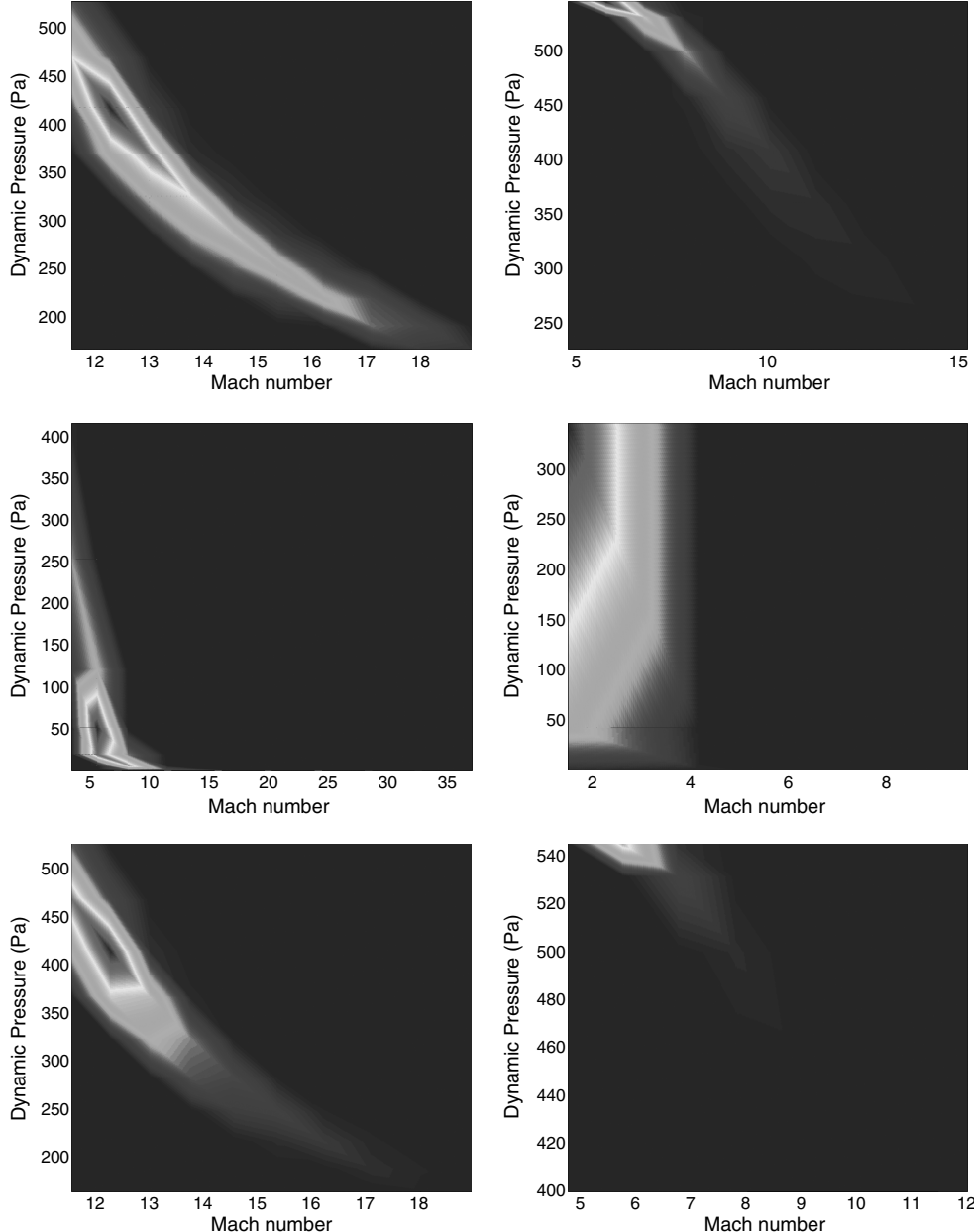


Fig. 16 Bivariate PDF of the Mach number and dynamic pressure (Pa) at $\tilde{t} = 0.30$ and 0.50 . First and second rows are three-state model with uniform and Gaussian initial PDF, respectively. The third row corresponds to the six-state model with uniform initial PDF.

where the definition of Lambert W function $x = W(x)e^{W(x)}$, has been used (see Appendix for details). Finally, the joint bivariate density in (M, q) is given by

$$\eta(M, q) = \frac{\xi(V^*, h^*)}{|\det(J^*)|} \quad (44)$$

where the right-hand side needs to be evaluated using Eqs. (41–43). Notice that, instead of using Lambert W function, one may also proceed by numerically solving Eq. (40).

Appendix lists the temperature model and associated numerics used in the simulation for computing the Mach number. The Mach- q bivariate marginals computed from Eq. (44) are plotted in Fig. 16 at $\tilde{t} = 0.30$ and 0.50 . The first row shows the plots for the three-state model with uniform initial condition uncertainty, the second row corresponds to the same model with Gaussian initial condition uncertainty. Plots in the last row are for the six-state model with uniform initial condition uncertainty and follow similar trend as the corresponding three-state case. With the Mach- q box dimension specified earlier, one can notice that for a three-state dynamics,

deploying a parachute at $\tilde{t} = 0.50$ will have significant reliability with Gaussian initial uncertainty compared with uniform initial uncertainty.

VII. Conclusions

A framework based on the SLE is provided for dispersion analysis in planetary EDL. It was argued that in this framework, one can do a systematic initial condition and parametric uncertainty analysis by spatio-temporally evolving the joint PDF through the SLE. Various analytical and numerical examples are given to illustrate how the MOC can be used to directly solve SLE, thereby making this framework not only computationally more tractable than traditional MC analysis, but also more accurate. For the EDL problem, results are provided for both three-state and six-state Vinh's equations for hypersonic entry in Mars atmosphere. Further, some case studies were presented to demonstrate how this framework naturally enables EDL specific statistical analysis. An initial implementation of the methodology described here, is now available in NASA Jet Propulsion Laboratory's DSEEDS simulator system for high-fidelity numerical experiments [41].

Appendix

I. Lambert W Function

The present section is intended to provide an overview of the Lambert W function. This function W is defined as the inverse of the function $f(W) = We^W$, where W is any complex number. The function satisfies the equation

$$W(z)e^{W(z)} = z \quad (\text{A1})$$

for every complex number z . This equation has infinite number of solutions, most of them being complex. Thus, W is a multivalued function. The different solutions of Eq. (A1) are called different *branches* of W , and are denoted as W_k . The index k takes its values from an index set \mathbb{Z} (the set of integers). Thus, different solutions or branches of Eq. (A1) are $W_0(z)$, $W_{\pm 1}(z)$, $W_{\pm 2}(z)$, etc. The case of particular interest is when the solution is real. Depending on the domain of W , one may have zero, one or two real solutions; in each case, the remaining solutions are complex. It is easy to see from Eq. (A1) that $W(x)$ is real, provided $x \in [-\frac{1}{e}, \infty) \subset \mathbb{R}$. Figure A1 shows how $W(x)$ varies with x . From the figure, it follows that when $x \in [-\frac{1}{e}, 0]$, W is double valued (two branches W_0 (solid) and W_{-1} (dashed)) and for $x \in [0, \infty)$, W is single valued (only W_0 branch). In other words, *unique real root* occurs only when the domain is restricted to the non-negative reals.

The readers are encouraged to refer the paper by Corless et al. [42] for an excellent account on Lambert W function from both theoretical and applied point of view. Two more significant references geared toward applications are [43,44].

II. Computing Mach Number

Case IV of Sec. VI discusses the quantification of chute deployment uncertainty by computing the Mach- q bivariate PDF. Equation (35) modeled the Mach number as $M = \frac{v}{\sqrt{\gamma R_* T(h)}}$. The

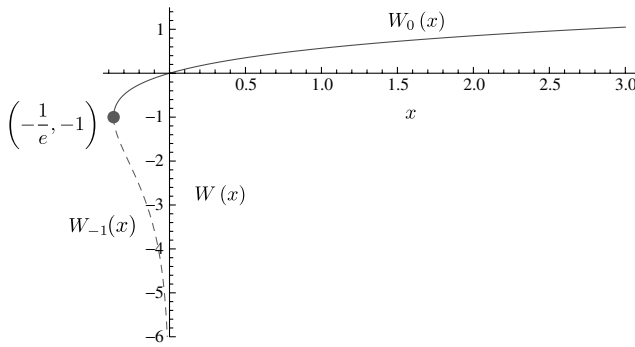


Fig. A1 Real-valued Lambert W function.

Table A1 Different types of molecular DOFs

Type	Number of translational DOF	Number of rotational DOF	Number of vibrational DOF
Linear molecule	3	2	$3n - 5$
Nonlinear molecule	3	3	$3n - 6$

denominator $\sqrt{\gamma R_* T(h)}$ represents the speed of sound. In this section, we describe how to compute the quantities γ , R_* , and $T(h)$ in the present context.

A. Modeling γ

The ratio of specific heats γ is modeled as

$$\gamma = \frac{f+2}{f} \quad (\text{A2})$$

with f being the total number of degrees-of-freedom (DOF) of the molecule, which is further given by $f = 3n$, where n is the number of atoms in a molecule. The contribution to total number of DOFs comes from three types, viz. translational DOFs, rotational DOFs, and vibrational DOFs; the amount of contribution from each type depends on whether the geometric arrangement of the atoms in the molecule are linear or nonlinear (see Table A1).

At low temperature, the vibrational DOFs are not excited. For example, terrestrial dry air, being primarily a mixture of diatomic gases (approx. 78% nitrogen and 21% oxygen), has only three translational and two rotational DOFs at low temperature. Hence $\gamma_{\text{air}}^{\text{low}} = \frac{5+2}{5} = 1.4$. But at high temperature, all $f = 3 \times 2 = 6$ DOFs are excited and $\gamma_{\text{air}}^{\text{high}} = \frac{6+2}{6} \approx 1.33$.

Atmosphere in Mars, being largely constituted of (approx. 95% by volume) triatomic carbon dioxide (a linear molecule), has five total molecular DOFs at low temperature and nine molecular DOFs at high temperature. In this paper, for the problem of hypersonic entry at upper Martian atmosphere (typically more than 7 km altitude), $\gamma = 1.4$ is considered while for supersonic descent through thicker (and warmer) atmosphere (below 7 km altitude), $\gamma = \frac{11}{9} \approx 1.22$ is assumed.

B. Modeling R_*

The difference between specific heats (R_*), sometimes called *specific gas constant*, is given by

$$R_* = \frac{R}{M} \quad (\text{A3})$$

where $R = 8.3145 \text{ J mol}^{-1} \text{ K}^{-1}$ is the *universal gas constant* and M is the *molar mass of the gas or gas mixture* (in kg mol^{-1}). For carbon dioxide, $M = 44.01 \times 10^{-3} \text{ kg mol}^{-1}$, which leads to $R_* = 188.9230 \text{ J kg}^{-1} \text{ K}^{-1}$ [using Eq. (A3)].

C. Modeling $T(h)$

In Mars atmosphere, the variation of temperature T with altitude h , usually termed as the *lapse rate*, can be modeled as the following piecewise linear function[‡]

$$T(h) = \begin{cases} -23.4 - 0.002220h & \text{for } h > 7000 \\ -31.0 - 0.000998h & \text{for } h < 7000 \end{cases} \quad (\text{A4})$$

where T is in deg Celsius and h is in meters.

Acknowledgments

This research work was supported by NASA Jet Propulsion Laboratory Director's Research and Development Fund DRDF-

[‡]Data available at <http://www.grc.nasa.gov/WWW/K-12/airplane/atmosmrm.html> [accessed June 2010].

FY09 with J. (Bob) Balaram (section 347) as Jet Propulsion Laboratory principal investigator and Aron Wolf (section 343) as Jet Propulsion Laboratory coinvestigator. In particular, we are thankful to Bob for many insightful discussions.

References

- [1] Braun, R. D., and Manning, R. M., "Mars Exploration Entry, Descent and Landing Challenges," *2006 IEEE Aerospace Conference*, IEEE Publications, Piscataway, NJ, 2006.
- [2] Steinfeldt, B. A., Theisinger, J. T., Korzun, A. M., Clark, I. G., and Braun, R. D., "High Mass Mars Entry, Descent and Landing Architecture Assessment," *2009 AIAA Space Conference*, AIAA Paper 2009-6684, 2009.
- [3] Spencer, D. A., and Braun, R. D., "Mars Pathfinder Atmospheric Entry: Trajectory Design and Dispersion Analysis," *Journal of Spacecraft and Rockets*, Vol. 33, No. 5, 1996, pp. 670–676.
doi:10.2514/3.26819
- [4] Desai, P. N., Braun, R. D., Powell, R. W., Engelund, W. C., and Tartabini, P. V., "Six-Degree-of-Freedom Entry Dispersion Analysis for the METEOR Recovery Module," *Journal of Spacecraft and Rockets*, Vol. 34, No. 3, 1997, pp. 334–340.
doi:10.2514/2.3213
- [5] Desai, P. N., Mitcheltree, R., and Cheatwood, F., "Entry Dispersion Analysis for the Stardust Comet Sample Return Capsule," *Journal of Spacecraft and Rockets*, Vol. 36, No. 3, 1999, pp. 463–469.
doi:10.2514/2.3467
- [6] Braun, R. D., Mitcheltree, R., and Cheatwood, F., "Mars Microprobe Entry-to-Impact Analysis," *Journal of Spacecraft and Rockets*, Vol. 36, No. 3, 1999, pp. 412–420.
doi:10.2514/2.3461
- [7] Striepe, S. A., Queen, E. M., Powell, R. W., Braun, R. D., Cheatwood, F., Aguirre, J. T., Sachi, L. A., and Lyons, D. T., "An Atmospheric Guidance Algorithm Testbed for the Mars Surveyor Program 2001 Orbiter and Lander," *AIAA Atmospheric Flight Mechanics Conference and Exhibit*, AIAA, Reston, VA, 1998.
- [8] Striepe, S. A., Way, D. W., Dwyer, A. M., and Balaram, J., "Mars Science Laboratory Simulations for Entry, Descent, and Landing," *Journal of Spacecraft and Rockets*, Vol. 43, No. 2, 2006, pp. 311–323.
doi:10.2514/1.19649
- [9] Knocke, P. C., Wawrzyniak, G. G., Kennedy, B. M., Desai, P. N., Parker, T. J., Golombek, M. P., Duxbury, T. C., and Kass, D. M., "Mars Exploration Rovers Landing Dispersion Analysis," *AIAA/AAS Astrodynamics Specialist Conference and Exhibit*, AIAA Paper 2004-5093, 2004.
- [10] Congdon, W. M., "Ablation Model Validation and Analytical Sensitivity Study for the Mars Pathfinder Heat Shield," *30th AIAA Thermophysics Conference*, AIAA, Washington, D.C., 1995.
- [11] Powell, R. W., Striepe, S. A., Desai, P. N., Queen, E. M., Tartabini, P. V., Brauer, G. L., Cornick, D. E., Olson, D. W., Petersen, F. M., Stevenson, R., Engel, M. C., and Marsh, S. M., "Program to Optimize Simulated Trajectories (POST II), Vol. II Utilization Manual," ver. 1.1.1.G, NASA Langley Research Center, Hampton, VA, May 2000.
- [12] Balaram, J., Austin, R., Banerjee, P., Bentley, T., Henriquez, D., Martin, B., McMahon, E., and Sohl, G., "DSENDS—A High Fidelity Dynamics and Spacecraft Simulator for Entry, Descent and Surface Landing," *2002 IEEE Aerospace Conference*, IEEE Publications, Piscataway, NJ, 2002.
- [13] Niederreiter, H., *Random Number Generation and Quasi-Monte Carlo Methods*, CBMS-NSF Regional Conference Series in Applied Mathematics, Society for Industrial and Applied Mathematics, Pennsylvania, 1992.
- [14] Regan, F. J., and Anandakrishnan, S. M., *Dynamics of Atmospheric Re-entry*, AIAA Education Series, AIAA, Washington, D.C., 1993, Chap. 13, pp. 425–475.
- [15] Spanos, P., and Ghanem, R., "Stochastic Finite Element Expansion for Random Media," *Journal of Engineering Mechanics*, Vol. 115, No. 5, 1989, pp. 1035–1053.
doi:10.1061/(ASCE)0733-9399(1989)115:5(1035)
- [16] Xiu, D., and Hesthaven, J., "High-Order Collocation Methods for Differential Equations with Random Inputs," *SIAM Journal on Scientific Computing*, Vol. 27, No. 3, 2005, pp. 1118–1139.
doi:10.1137/040615201
- [17] Debusschere, B. J., Najm, H. N., Pébay, P. P., Knio, O. M., Ghanem, R. G., and Le Maître, O. P., "Numerical Challenges in the Use of Polynomial Chaos Representations for Stochastic Processes," *SIAM Journal on Scientific Computing*, Vol. 26, No. 2, 2004, pp. 698–719.
doi:10.1137/S1064827503427741
- [18] Prabhakar, A., Fisher, J., and Bhattacharya, R., "Polynomial Chaos Based Analysis of Probabilistic Uncertainty in Hypersonic Flight Dynamics," *Journal of Guidance, Control, and Dynamics*, Vol. 33, No. 1, 2010, pp. 222–234.
doi:10.2514/1.41551
- [19] Marchisio, D. L., and Fox, R. O., "Solution of Population Balance Equations using the Direct Quadrature Method of Moments," *Journal of Aerosol Science*, Vol. 36, No. 1, 2005, pp. 43–73.
doi:10.1016/j.jaerosci.2004.07.009
- [20] Shohat, J. A., and Tamarkin, J. D., *The Problem of Moments*, Mathematical Surveys and Monographs, American Mathematical Society, New York, 1943, Chap. 1, pp. 1–22.
- [21] Mura, A., and Borghi, R., "Introducing A New Partial PDF approach for Turbulent Combustion Modeling," *Combustion and Flame*, Vol. 136, No. 3, 2004, pp. 377–382.
doi:10.1016/j.combustflame.2003.10.004
- [22] Silverman, B. W., *Density Estimation for Statistics and Data Analysis*, Monographs on Statistics and Applied Probability, 26, Chapman and Hall, London, 1994.
- [23] Pantano, C., and Shotorban, B., "Least-squares Dynamic Approximation Method for Evolution of Uncertainty in Initial Conditions of Dynamical Systems," *Physical Review E (Statistical Physics, Plasmas, Fluids, and Related Interdisciplinary Topics)*, Vol. 76, No. 6, 2007, pp. 066705-1–066705-13.
doi:10.1103/PhysRevE.76.066705
- [24] Ehrendorfer, M., "The Liouville Equation and its Potential Usefulness for the Prediction of Forecast Skill. Part I: Theory," *Monthly Weather Review*, Vol. 122, No. 4, 1994, pp. 703–713.
doi:10.1175/1520-0493(1994)122<0703:TLEAIP>2.0.CO;2
- [25] Khalil, H. K., *Nonlinear Systems*, 3rd ed., Prentice Hall, NJ, 2002, Chap. 3, pp. 93–98.
- [26] Lasota, A., and Mackey, M., *Chaos, Fractals and Noise: Stochastic Aspects of Dynamics*, Applied Mathematical Sciences, Vol. 97, Springer-Verlag, New York, 1994, Chap. 3, pp. 37–49.
- [27] Epstein, B., *Partial Differential Equations*, McGraw-Hill, New York, 1962, Chap. 2, pp. 36–41.
- [28] Delgado, M., "The Lagrange-Charpit Method," *SIAM Review*, Vol. 39, No. 2, 1997, pp. 298–304.
doi:10.1137/S0036144595293534
- [29] Babelon, O., Bernard, D., and Talon, M., *Introduction to Classical Integrable Systems*, Cambridge Univ. Press, Cambridge, England, 2003, Chap. 3, pp. 32–85.
- [30] Gaspard, P., *Chaos, Scattering and Statistical Mechanics*, 1st ed., Cambridge Univ. Press, Cambridge, England, 1998, Chap. 3, pp. 67–125.
- [31] Ehrendorfer, M., "The Liouville Equation and Atmospheric Predictability," *Predictability of Weather and Climate*, edited by T. Palmer, and R. Hagedorn, Cambridge Univ. Press, Cambridge, England, 2006, pp. 59–98.
- [32] Arnold, V. I., *Mathematical Methods of Classical Mechanics*, translated by K. Vogtmann, and A. Weinstein, 2nd ed., Springer, Berlin, 1989, Chap. 3, pp. 55–74.
- [33] Vinh, N. X., Busemann, A., and Culp, R. D., *Hypersonic and Planetary Entry Flight Mechanics*, Univ. of Michigan Press, Ann Arbor, MI, 1980.
- [34] Noton, M., *Spacecraft Navigation and Guidance*, Advances in Industrial Control, Springer-Verlag, New York, 1998, Chap. 7, pp. 141–144.
- [35] Halder, A., and Bhattacharya, R., "Beyond Monte Carlo: A Computational Framework for Uncertainty Propagation in Planetary Entry, Descent and Landing," *AIAA Guidance, Navigation and Control Conference*, AIAA, Reston, VA, 2010.
- [36] Devroye, L., *Non-uniform Random Variate Generation*, Springer-Verlag, New York, 1986.
- [37] Gilks, W. R., Richardson, S., and Spiegelhalter, D., *Markov Chain Monte Carlo in Practice*, Interdisciplinary Statistics, Springer-Verlag, New York, 2007.
- [38] Chib, S., and Greenberg, E., "Understanding the Metropolis–Hastings Algorithm," *The American Statistician*, Vol. 49, No. 4, 1995, pp. 327–335.
doi:10.2307/2684568
- [39] Diaconis, P., "The Markov Chain Monte-Carlo Revolution," *Bulletin of the American Mathematical Society*, Vol. 46, No. 2, 2008, pp. 179–205.
doi:10.1090/S0273-0979-08-01238-X
- [40] Andrieu, C., Freitas, N. D., and Jordan, M. I., "An Introduction to MCMC for Machine Learning," *Machine Learning*, Vol. 50, Nos. 1–2, 2003, pp. 5–43.
doi:10.1023/A:1020281327116

- [41] Balaram, J., Bhattacharya, R., and Halder, A., "Beyond Monte-Carlo: Statistical Verification and Validation of Space Systems," NASA Jet Propulsion Laboratory DRDF Final Rept. 1328, 2010.
- [42] Corless, R. M., Gonnet, G. H., Hare, D. E. G., Jeffrey, D. J., and Knuth, D. E., "On the Lambert W Function," *Advances in Computational Mathematics*, Vol. 5, No. 1, 1996, pp. 329–359.
doi:10.1007/BF02124750
- [43] Valluri, S. R., Jeffrey, D. J., and Corless, R. M., "Some Applications of the Lambert W Function to Physics," *Canadian Journal of Physics*, Vol. 78, No. 9, 2000, pp. 823–831.
doi:10.1139/cjp-78-9-823
- [44] Packel, E. M., and Yuen, D. S., "Projectile Motion with Resistance and the Lambert W Function," *The College Mathematics Journal*, Vol. 35, No. 5, 2004, pp. 337–350.